This document is the accepted manuscript version of the following article:

Pillatsch, L., Kalácska, S., Maeder, X., & Michler, J. (2021). In situ atomic force microscopy depth-corrected three-dimensional focused ion beam based time-of-flight secondary ion mass spectroscopy: spatial resolution, surface roughness, oxidation. Microscopy and Microanalysis, 27(1), 65-73. https://doi.org/10.1017/S1431927620024678

In situ atomic force microscopy depth-corrected 3-dimensional focused ion beam based time-of-flight secondary ion mass spectroscopy: spatial resolution, surface roughness, oxidation

Lex Pillatsch[a,b], Szilvia Kalácska[a*] , Xavier Maeder[a], Johann Michler[a]

[a]*Empa, Swiss Federal Laboratories for Materials Science and Technology, Laboratory of Mechanics of Materials and Nanostructures,*

CH-3602 Thun, Feuerwerkerstrasse 39. Switzerland

[b]*TOFWERK AG., CH-3600 Thun, Uttigenstrasse 22 Switzerland*

*Corresponding Author's *Email address: szilvia.kalacska@empa.ch, Tel.: +41 58 765 626, Fax: +41 58 765 6990*

Abstract

Atomic force microscopy (AFM) is a well-known tool for studying surface roughness and to collect depth information about features on the top atomic layers of samples. By combining secondary ion mass spectroscopy (SIMS) with focused ion beam (FIB) milling in a scanning electron microscope (SEM), chemical information of sputtered structures can be visualized and located with high lateral and depth resolution. In this paper, a high vacuum (HV) compatible AFM was installed in a TESCAN FIB-SEM instrument that was equipped with a time-of-flight secondary ion mass spectroscopy (ToF-SIMS) detector. To calibrate the sputtering rate and measure the induced roughness caused by the ToF-SIMS sputtering, subsequent AFM measurements were performed on an inorganic multilayer vertical cavity surface emitting laser (VCSEL) sample. Normalized sputtering rates were used to aid accurate 3D reconstruction of the sputtered volume's chemical composition.

Achievable resolution, surface roughness during sputtering and surface oxidation issues were analysed. The integration of complementary detectors opens up the ability to determine the sample properties as well as to understand the influence of the Ga^+ ion sputtering method on the sample surface during the analysis.

Keywords: time of flight secondary ion mass spectroscopy (TOF-SIMS), atomic force microscopy (AFM), tomography, depth profiling, focused ion beam (FIB), chemical characterization

1. Introduction

Focused ion beam secondary ion mass spectroscopy (FIB-SIMS) is a well-known surface analysis technique [Dunn 1999][Giannuzzi 2005][Giannuzzi 2011]. The measurement principle is based on locally sputtering the sample by impacting ions while collecting and selecting the sputtered ions according to their mass. The sensitivity of SIMS makes it suitable for locating trace elements important to detect impurities in semi-conductors and metals. SIMS is also capable of analysing the chemical composition of multilayer structures [Whitby 2012] with an excellent depth resolution. The remarkable depth resolution comes from the localization of sputtered particles that are limited to the few top surface layers [Pillatsch 2018][Priebe 2019]. Although SIMS is extremely surface sensitive, it is not possible to determine the depth of a sputtered particle as the sputter rate depends on the chemical and crystallographic composition of the sample and the projectile. Therefore, the elemental composition of the sputtered volume is usually represented as signal per sputtered frame. This often leads to a false impression of the depth-represented elemental composition. Depth profiling of the crater after SIMS measurement gives only information about the average sputtering rate of the analysed volume,

which can vary significantly because of the different sputtering rates of the analysed structures at various crater depths.

An additional analysis method is required to calibrate the depth of the sputtered crater and to analyse the roughness of the crater bottom. This information is provided by atomic force microscopy (AFM). There have been previous attempts to couple AFM and ToF-SIMS analysis to carry out depth profile analysis [Busby 2018, Casula 2019] and surface roughness characterization by AFM [Noel 2019]. When combining AFM with SIMS, the AFM needs to be vacuum compatible as SIMS measurements are done in high vacuum (HV). Breaking the vacuum for AFM measurement needs to be avoided when alternating SIMS and AFM measurements as surface oxidation can occur. A suitable HV AFM setup that is easy to implement is based on a tuning fork AFM where the tip vibration is controlled and recorded by tracking the variations in the electrical impedance of the tuning fork [Akiyama 2006][Akiyama 2003a][Akiyama 2010][Akiyama 2003b]. No optical setup is required for this type of AFM, which makes it easy to adjust in vacuum.

An advantage of *in situ* AFM consists in a higher quality factor (Q-factor) compared to in-air AFM. The Q-factor of a micro-cantilever AFM probe is defined as

$$Q=f_0/\Delta f,$$

where Δf = (full-width at maximum height/$\sqrt{2}$) of the resonance peak of the amplitude curve, while f_0 is the resonance frequency [Perez-Cruz2012]. This Q-factor indicates the damping and the energy dissipation capacity of the applied system.

The damping force from ambient air acting on the vibration of the tip is missing in vacuum, which allows free vibration of the tip hence the Q-factor is increased. The consequence of a high Q factor is faster response reaction to variation of the tip-to-surface interaction [Kushmeric 2016] and thus the sensitivity to surface variations is higher.

At ambient pressure, the AFM can be driven either in amplitude mode (AM-AFM) by keeping the amplitude of the tip vibration constant, or in frequency mode (FM-AFM) by keeping the frequency of the tip vibration constant. Both methods are used in tapping mode where although the tip is close to the surface, but any actual contact between surface and tip should be avoided. For AM-AFM, the frequency of the tip changes according to the interaction force between the tip and the surface. The frequency shift of the tip is proportional to the scan speed and inversely proportional to the Q-factor [Kushmeric 2016][Rodríguez 2003]. Apart from measuring the surface height, AM-AFM mode also provides information about the presence of different domain segregations by tracking the phase shift between the vibration frequency and the excitation frequency of the tip, that is proportional to the tip-surface interaction force [Bayat 2008]. A drawback of this measurement method is the link of the Q-factor to the scan speed. In HV conditions, the elevated Q-factor leads to a reduced scan speed in order to keep the tip vibration in an acceptable frequency range for a given tip vibration amplitude. This will slow down the scan speed to an unacceptable level.

For FM-AFM, the Q-factor is independent from the scan speed. Frequency detection is not affected by the amplitude of the tip vibration. This allows maintaining high scan speeds while recording precise information of the surface height. As phase shift cannot be measured, the composition of the surface cannot be tracked by this method. Nevertheless, the FM-AFM precision in terms of depth measurement is higher than the precision of the AM-AFM mode.

Visualization of the crater was done by SEM after the last AFM scan. The SEM image is useful to determine and overlay the scan area of the earlier AFM and SIMS measurements and to confirm the measured AFM data after surface sputtering.

In this article, we present a scanning strategy to alternate AFM and SIMS measurements in order to get the depth information about the chemical composition of a multilayer sample. Advantages and drawbacks of the acquisition are analysed and limits of the measurement are discussed.

2. Materials and Methods

A FIB-SEM instrument developed by TESCAN served as platform for the SIMS-AFM integration. The sample was sputtered by a gallium (Ga^+) FIB. Surface damage induced by the impacting Ga^+ ions was visualized by SEM pictures. The elemental composition of the sample-was measured by an orthogonal ToF-SIMS instrument [Alberts 2014] developed by TOFWERK AG (Switzerland). This configuration allows using a continuous Ga^+ ion beam for the simultaneous sputtering and analysis process. With the HV compatible AFM the surface roughness and the sputter depth in between the SIMS scans were measured.

2.1. AFM setup

Figure 1 shows the AFM setup with a tuning fork tip that was designed to fit in the FIB-SEM instrument. For the so-called “Akiyama tips” the silicon (Si) tip apex is attached between two prongs [Akiyama 2010]. The deflection of the tip, orthogonal to the vibration plane of the prongs, is induced by periodical changing of the mechanical stress in the legs of the cantilever. The tuning fork itself acts as an oscillatory force sensor and dominates the frequency and the amplitude of the tip vibration. The interaction of the tip with the surface was measured by the piezoelectric current of the tuning fork. Important parameters of the AFM measurements are summarized in Table 1. The resonance frequency of the tip was about 45 kHz with Q-factor measured in air of about 1000. In vacuum, the tip vibration was not damped by air. The Q-factor in this case was 4-5 times higher which

had a favourable impact on the reaction precision of the tip height. AFM measurements were performed in FM-AFM tapping mode. The compactness of the AFM setup allowed mounting the AFM tip between the extraction optics of the ToF-SIMS, the FIB and the sample surface. The sample was mounted on the AFM piezo scanner with a maximum scan range of 10 µm × 10 µm. For a 512 px × 512 px scan with a lateral resolution of 20 nm and a scan speed of 1.5 s/line, an AFM scan took about 13 minutes. The height adjustment of the tip was done by a piezo scanner below the tip with a maximum movement range of 5 µm. The coarse motion of the tip was done by a tripod setup of slip stick actuators. The coarse motion was independent of the AFM scanner and served only to set the tip at the area of interest and so to intersect the tip scan area with the scan area of the SIMS. During the actual AFM scan, the tip height was regulated by a piezo actuator under the AFM tip. Statistical analysis of each AFM measurement was carried out on a 5 µm × 5 µm area applying a raster size of 128 px × 128 px.

Force constant of the cantilever	5 N/m
Apex radius of the tip	~15 nm
Applied mode	FM-AFM tapping
AFM maximum scan range	10 µm × 10 µm
AFM lateral resolution	20 nm (512 px × 512 px)
Scan speed	1.5 s/line
Repetition positioning error	~100 nm
Time to switch from AFM to SIMS	10 s
AFM tip positioning time	Under 3 minutes

Table 1: Parameters of the AFM measurements.

2.2. **SIMS**

The SIMS measurements were carried out with a high-resolution ToF-SIMS detector from TOFWERK AG, Thun, Switzerland [Whitby 2012]. The mass resolution of the orthogonal ToF-SIMS was $\Delta m/m > 3900$ Th/Th, where Δm denotes the peak width at full-

width at half-maximum (Th is the unit 'Thomson' for charge to mass ratio). The sample was sputtered by the Ga^+ beam perpendicular to the sample surface. The beam of sputtered particles is pulsed in orthogonal direction in the ToF-SIMS mass analyser. This configuration allows to use the same continuous beam for sputtering and analysing the sample with ToF-SIMS. Beam energy of 20 keV was chosen for both sputtering and analysis in order to guarantee a lateral resolution below 50 nm [Whitby 2012][Alberts2014]. The extraction voltage for the secondary ions applied to the extraction nozzle of the ToF-SIMS was limited to < 200 V, while the sample itself was grounded. The distance between the extraction optics and the sample surface was 9 mm. Because of the weak electric field, the AFM tip could stay at a distance of about 20 µm from the scanning area without disturbing the ion extraction of the ToF-SIMS. Therefore, it was possible to make fast alternation between SIMS and AFM scans with a repetition precision in the range of 100 nm that was limited by the coarse motion for the tip positioning.

2.3. **SEM**

The exact location of the tip and the distance between the sample surface and the AFM tip was visualized by SEM. As the magnification of the SEM is higher by orders of magnitude than for optical microscopes, approaching and positioning of the tip at the area of interest was easy. Furthermore, damage of the apex of the tip was noted prior to AFM measurements. If the AFM parameters were adjusted adequately, the tip apex would last during several AFM scans which was required for a correct AFM-SIMS reconstruction of the sample. The position of the scan area of the AFM measurement matching the position of the crater done by the FIB beam can be determined by SEM in case the intersection of the FIB and the SEM beam is done correctly at the sample surface. SEM was also applied

to visualize the sputter location after the SIMS-AFM measurement to confirm the correctness of the AFM data.

2.4. Sample

The concept of depth calibration of the SIMS depth profile with direct depth measurements by AFM was demonstrated on a multilayer vertical cavity surface emitting laser (VCSEL) sample [Lyytikäinen 2009]. The exact layer structure of the sample is shown in Figure 2 a). This sample was chosen because of its initial surface flatness and its elemental composition being favourable for SIMS measurements.

The well-defined layer structure with the discrete border limitation was ideal to measure the intermixing due to collision cascades induced by impacting ions. Figure 2 b) shows the SIMS depth profile of ^{27}Al, ^{69}Ga and ^{115}In as a function of the SIMS frames.

2.5. Numerical control of the SIMS-AFM combination

The SIMS-AFM combination is either used to determine the surface roughness and the crater depth at a specific SIMS frame or the SIMS-AFM scans are alternated, giving a 3D data set with the real sputter depth. The alternation of the SIMS-AFM scans was controlled through a Python script. The script only took over control when switching between SIMS and AFM, so to start and stop a SIMS acquisition, to relocate the AFM tip before and after a SIMS acquisition (Figure 3 a) and to launch the AFM scans. The SIMS- and AFM-specific parameters such as scan range, scan speed, resonance frequency of the AFM tip were all set in the software of the corresponding analysis tool. New SIMS data acquisition was launched after each AFM acquisition set, resulting in several SIMS data sets that could be handled together by an external software. The periodicity of alternation between SIMS and AFM was determined by the number of SIMS frames per SIMS data set.

2.6. SIMS-AFM scanning strategy

During the overall SIMS-AFM experiments, AFM measurements were the most time consuming. As the AFM tip was scanning line by line with a defined scan speed, the scan time increased with the power of 2 with the increase of the scan area for a given lateral resolution. For the analysed sample a SIMS scan area of 10 µm × 10 µm was enough to get the required information about the chemical composition of the different layers. This scan size was on the edge of the scanning range of the AFM setup.

A time efficient scanning strategy leading to collect depth and roughness information at the centre of the crater consisted of two AFM scans (Figure 3 b and c). The inner part of the SIMS crater was measured first by an AFM scan to record the roughness of the crater bottom. A second AFM scan with the crater edge in the middle of the scan area measured the sputter depth of the crater. By overlaying both AFM scans, all the required information could be extracted. Crater depths were determined by the Gwyddion software [Nečas 2012].

3. Results

3.1. Surface oxidation

It took ~25 minutes to perform the overall AFM analysis on the crater after each ToF-SIMS measurement. With a pressure $p = 10^{-6}$ mbar in the analysis chamber and by assuming that the residual gas in the FIB-SIMS-SEM instrument consisted only of N_2 molecules (the chamber was vented with nitrogen when changing the sample) the number of impinging atoms at the analysis surface during the AFM scan was calculated by [Jeans 2009]:

$$N_{mol} = \frac{p}{\sqrt{2\pi m k_B T}}, \quad (1)$$

where m is the molecular mass of N_2 molecules, k_B is the Boltzmann constant an T = 298 K is the ambient temperature, resulting N_{mol} = 2.9×10^6 molecules/µm^{2}s impinging nitrogen molecules. Within 25 minutes, 4.3×10^9 molecules/µm^2 would impinge a surface unit. This is sufficient to cover the surface. Whereas only N_2 molecules were assumed to be in the residual gas, in reality, a non-negligible fraction of chemically more reactive molecules (O_2, H_2O, C_2, ...) were contained as well in the residual gas. These reactive molecules would react with the surface during the AFM scan. Of course, only a given fraction of impinging molecules can react with the surface and therefore have an effect on the chemical surface state.

The ionisation probability of sputtered particles (and so the secondary ion signal) depends on the chemical state of the surface. The effect of surface oxidation enhances the secondary ion formation, and as a result, the signal of the first SIMS frame recorded after an AFM scan was significantly higher. Already at the subsequent SIMS scan, most of the oxidized surface was sputtered away, resulting in SIMS signal drop, appropriate to a clean surface. In Figure 4 the effect of surface oxidation on the SIMS signal after the AFM scan (every twentieth SIMS frame) is visible.

Being aware of this effect, the signal spikes were eliminated by averaging over the last secondary ion signal before and the ion signal of the second SIMS frame after an AFM scan in order to reflect the SIMS depth profile in absence of surface oxidation. This correction was found to be necessary to eliminate a false periodic signal appearing on the 3D reconstructions in Section 4 in order to visualize the real structure and composition of the sample.

The depth profile of the VCSEL sample was recorded by SIMS. Beginning with an AFM scan, the SIMS depth profile was interrupted at every 20th frames to measure the sputter depth and the crater roughness by AFM.

Figure 5 shows the results of the combined SIMS-AFM measurement. The concentration variation of aluminium ions (^{27}Al), gallium ions (^{69}Ga) and indium ions (^{115}In) in the layer structure of the VCSEL is reflected by the SIMS depth profile. The sputter rate per 20 SIMS frames of the sample varies as a function of the local sample composition.

In Figure 6 the correction of the sputter depth of the ^{27}Al signal by AFM measurements is compared to the depth profile related directly to the sputter time of the crater. When referring the ^{27}Al signal to the sputter time, the layer thickness is reflected incorrectly due to the involved unknown sputter rate of the different layers. This is clearly visible in Figure 4 by the mismatch between the ^{27}Al signal once represented as a function of the sputter time and once represented by a correct depth calibration of the sputtered crater.

Starting with a roughness of 100 nm of the pristine surface, the decreasing trend of the roughness was observed until the 18th AFM scan (InP layer). The initial surface roughness was reduced by sputtering without adding new roughness by the impacting ions. The variation of the root mean square (RMS) roughness of the crater bottom for the AFM scans 18 (InP layer) to 26 (AlGaAs-GaAs layer structure) is related to the globular nanostructure formation at the surface (Figure 7).

4. Discussions

The sputter process of a sample by an incident ion beam depends on the sample configuration, the used incident ions, and the sample-incident ion beam interaction. The sputter rate is thus dependent on the layers to be sputtered, the mixing of the layers at the interface and the implantation and chemical reaction of incident ions with the sample

and the development of the roughness related to the sputter process. The nature of incident ions, cluster or mono atomic ion beam, influences the sputter behaviour. The acceleration energy distributed between atoms of a cluster results in lower impact energy per atom and thus in a higher energy deposition close to the surface for clusters. Therefore, the use of cluster bombardment in a given energy range is beneficial for a high sputter rate.

4.1. Sputter rate and roughness analysis by AFM

In Figure 5 it can be noticed that the sputter rate is highest on the falling slope of SIMS signals of the ^{115}In-rich layers (AFM scans 3, 5 and 8: the interface between InP - AlGa) than on its corresponding rising slope (AFM scans 4, 6, 9, 12 and 15: within the layer AlGaInAs). This indicates that the sputter behaviour was influenced by the interlayer mixing. The sputtering of one of the ^{27}Al-rich structure (AFM scans 7, 10 and 15: within the layer AlGaInAs) is lower than the sputtering rate at the AlGaInAs/InP interfaces, but still higher than the sputtering rate of InP (AFM scan 17 and 18).

As the sputter behaviour of the sample was unknown prior to measurement, it was not possible to synchronize the depth measurements with the SIMS signals. Nevertheless, it was possible to determine the consistency of the sputter rate of an ^{27}Al-rich layer structure by summing up the sputter depth of three consecutive AFM measurements incorporating an ^{27}Al-rich layer structure (Figure 5). For all 5 ^{27}Al-rich structures the same amount of material was sputtered away. For the first ^{27}Al rich layer structure, the sputter depth of 177 nm was influenced by the foregoing AlInAs/InP layers as well as by the initial surface roughness. The sputter depth of 170 nm of the second ^{27}Al-rich structure was still influenced by the high roughness of the surface. With the decreasing roughness, the sputter depth for an ^{27}Al-rich layer levelled off to about 145-155 nm for the 3–

5 ^{27}Al-rich structure. This corresponds to the distance between two ^{27}Al-rich layers defined during the production of the sample.

The crater depth shown in the top graph of Figure 5 increases constantly up to the 18th AFM scan (InP layer), just before reaching the AlGaAs-GaAs layer structure. The sputter rate for this layer structure defers noticeably from the previous layer structure, resulting in a lower sputtering behaviour, and thus in a lower sputter depth per 20 SIMS frames.

4.2. Surface roughness

In Figure 7 on the left side of the 18th AFM scan (InP layer), the formation of an induced topography with a morphology characterised by globular nanostructures starts already. When comparing the depth of the AFM scans with the SIMS data, globular nanostructure formation occurs mainly on the GaAs/AlGaAs interface. At the AFM scan 19 (the interface between InP - AlGaAs-GaAs layer structure) well separated globular nanostructures are formed. The low RMS roughness values are still dominated by the flat surface area in between the globular nanostructures. The RMS roughness increases at the AFM scan 20 (AlGaAs-GaAs layer structure) due to the expansion of the globular nanostructures. When the GaAs/AlGaAs interface appears, the globular nanostructures are sputtered and a more uniform surface appeared. This leads to a reduction of the RMS roughness at the AFM scan 21-23 (AlGaAs-GaAs layer structure), just before a new GaAs/AlGaAs interface appears and the globular nanostructure formation starts again to dominate the surface structure. The globular nanostructure formation continues, leading to an increase of the RMS values. As stated in the article of Wei et al. [Wei 2008] the mechanism of globular nanostructure formation on a GaAs surface can be attributed to preferential sputtering of ^{75}As and clustering of the remaining excess of Ga^+, both form the Ga^+ beam and from the substrate. They also identified the composition of the globular

nanostructures by EDS and TEM to be pure ^{69}Ga. According to TRIM2013 simulations the sputtering yield of ^{75}As is 2.5 times higher than for ^{69}Ga. On the other hand, no local increase in ^{69}Ga could have been observed on SIMS images while globular nanostructures are formed. This can be explained by the movement of the globular nanostructures during sputtering and by Ga^+ induced nanostructures clouded out by the ^{69}Ga from the GaAs layer. The position of the globular nanostructures changes from frame to frame but the ^{69}Ga signal of the ToF-SIMS image was averaged over 20 frames. This is enough time for the globular nanostructures to move over the entire sputtered area. Although the globular nanostructures are a local accumulation of ^{69}Ga, the ^{69}Ga concentration around the globular nanostructures was still in the 10th of percent range as ^{69}Ga is present in the sample and the dose of Ga^+ implanted by the Ga^+ beam was high. The difference in ^{69}Ga signal coming from globular nanostructures and from the area around the globular nanostructures might therefore only be minor. It is important to note that it is not possible to determine the ^{69}Ga distribution of a sample sputtered by a Ga^+ beam containing the ^{69}Ga isotope. On the other hand, the ^{69}Ga signal should increase for layers containing ^{69}Ga, hence differences between ^{69}Ga-rich layers and layers without ^{69}Ga can still be distinguished from each other.

4.3. 3D reconstruction

To compensate for the difference in sputtering rate for subsequent layers, the AFM data was used to create a depth-calibrated data set for the 3D reconstruction. Between each AFM measurement, the surface was sputtered during 20 frames to acquire ToF-SIMS data. The sputter rate of different layers was changing significantly, but only the sputtered depth between two AFM layers was measured, leading to an average sputter rate between two AFM measurements. For the 3D reconstruction, the ToF-SIMS data had to

be split up again to 20 nm thick slices. With a fixed 20 nm depth and a variating sputter rate, the number of ToF-SIMS frames is adapted to correspond to the 20 nm depth. With a 20 nm depth of each slice and a total sputter depth of the measurement of 1.1 µm, 56 individual slices containing an integrated and normalized signal intensity measured by ToF-SIMS were formed. The intensity distribution of the elements of the entire measurement with respect to the actual sputter depth was done by pilling up the 56 slices. It is worth mentioning that for the sake of the 3D reconstruction, a different depth could have been chosen (bigger or smaller than 20 nm), but given that the created 56 layers were sufficiently showing the characteristics of the investigated structure, the value of 20 nm depth was set.

In Figure 8 the construction of three 3D model slices from the ToF-SIMS frames are shown. Voxel size in the 3D model is therefore 156 nm × 156 nm × 20 nm, as the ToF-SIMS mapping was binned to 64 pixel × 64 pixel resolution on a 10 µm × 10 µm area. In Figure 9 the 3D models reconstructed with Visage Imaging Amira 5.2.2 software are shown for the three studied ions.

The lateral size was cropped to 5 µm × 5 µm to get rid of the errors due to the edge effect (atoms from the side walls can contribute to the measured signal). For an easier interpretation of the distribution of secondary ions in depth, the Z axis has been exaggerated 6 times, in reality this axis corresponds to a depth of 1.1 µm.

From the 3D models, we can observe the five consequent $Al_xGa_{1-x}In_yAs_{1-y}$ – InP layers in the distribution of the three ions. This is in good agreement with the composition of the material (green dotted line in Figure 2). It is also clear that the bottom part (red dotted line in Figure 2) does not contain any ^{115}In, and that there is a difference in thickness between the ^{27}Al and ^{69}Ga bottom layers due to the existing GaAs layer above the

$Al_{0.9}Ga_{0.1}As$ layer. The intensities of ^{27}Al and ^{69}Ga ions are higher in this region compared to the upper layers.

In some regions secondary ions cannot be clearly distinguished (in example ^{115}In inside the InP layers). This is due to the matrix effect, when interactions between the ion and its surroundings can substantially alter the yield and type of ions that we can observe.

5. Summary and conclusions

One of the challenges for ToF-SIMS to be considered as an efficient 3D technique is to be able to accurately determine the depth from where the signal came from. The proposed combination of AFM and ToF-SIMS techniques takes us closer to achieve signal depth localization. It was demonstrated that consecutive sputtering and surface measuring can be successfully applied on materials which are ordered in an epitaxial manner. The concept of depth calibration of the SIMS depth profile by direct AFM depth measurements was demonstrated in this paper on a multilayer sample. SIMS-AFM scans of 10 μm × 10 μm area were alternated and controlled by a Python script.

Surface oxidation artefacts on SIMS profiles were corrected by averaging SIMS signals before and after AFM scans in order to reflect the real ion depth profiles. The concentration variations of ^{27}Al, ^{69}Ga and ^{115}In ions in the layer structure of the VCSEL sample show good agreement with the expected composition, however without the depth calibration SIMS depth profiles do not coincide with the known structure. Sputter rate varies as a function of the local sample composition. We noticed higher sputter rates on the falling slopes of SIMS signals of the ^{115}In-rich layers than on the corresponding rising slopes that indicates interlayer-mixing dependence of the sputter behaviour.

AFM scans showed globular nanostructure formation on the surface as a consequence of FIB milling. ^{69}Ga globular nanostructure formation has been observed by measuring the root mean square roughness values. It was concluded that the beginning of the globular nanostructure formation can be linked to a specific interface (the interface between InP - AlGaAs-GaAs layer structure). While both AFM scans and SEM imaging confirmed the induced topography with a morphology characterised by globular nanostructure formation, SIMS data of ^{69}Ga top projection showed no local increase in ^{69}Ga ion intensity.

3-dimensional depth corrected models of the sputtered material were successfully reconstructed using SIMS layers corresponding to 20 nm thick slices. AFM data could also be used to correct small surface roughness changes, leading to the composition of real 3D data sets, but it would require that an AFM scan is taken after every ToF-SIMS frame, but this would imply signal variation of every ToF-SIMS scan due to surface oxidation.

It was out of the scope of this work to consider real 3D data set correction for small roughness changes (in the order of couple of tens of nanometers) in case of the VCSEL sample. For samples with a more complex surface topology, due to the sputter rate that depends on local composition variation having an impact on the SIMS signal, it would be mandatory to take into account the roughness effects for an adequate representation of the sample structure.

Acknowledgement

The present work was supported by ROTTOF project 5211.01371.900.01 and by the EMPAPOSTDOCS-II programme (SzK), part of the European Union Horizon 2020 research and innovation programme under the Marie Slodowska-Curie grant agreement number 754364.

References

[Akiyama 2003a] T. Akiyama, U. Staufer, and N. de Rooij. (2003) "Self-sensing and self-actuating probe based on quartz tuning fork combined with microfabricated cantilever for dynamic mode atomic force microscopy," *Appl. Surf. Sci.*, vol. 210, no. 1–2, pp. 18–21, Mar.

[Akiyama 2003b] T. Akiyama, U. Staufer, N.F. de Rooij, P. Frederix, and A. Engel. (2003) "Symmetrically arranged quartz tuning fork with soft cantilever for intermittent contact mode atomic force microscopy," *Rev. Sci. Instrum.*, vol. 74, no. 1, p. 112.

[Akiyama 2006] T. Akiyama, K. Suter, N.F. de Rooij, A. Baumgartner, A.E. Gildemeister, T. Ihn, K. Ensslin, U. Staufer. (2006) "Scanning Probe with Tuning Fork Sensor, Microfabricated Silicon Cantilever and Conductive Tip for Microscopy at Cryogenic Temperature," *Jpn. J. Appl. Phys.*, vol. 45, no. 3B, pp. 1992–1995, Mar.

[Akiyama 2010] T. Akiyama, N.F. de Rooij, U. Staufer, M. Detterbeck, D. Braendlin, S. Waldmeier, and M. Scheidiger. (2010) "Implementation and characterization of a quartz tuning fork based probe consisted of discrete resonators for dynamic mode atomic force microscopy.," *Rev. Sci. Instrum.*, vol. 81, no. 6, p. 063706, Jun.

[Alberts 2014] D. Alberts, L. von Werra , F. Oestlund , U. Rohner, M. Hohl , J. Michler, J.A. Whitby. (2014) "Design and Performance of Two Orthogonal Extraction Time-of-Flight Secondary Ion Mass Spectrometers for Focused Ion Beam Instruments," *Instrum. Sci. Technol.*, vol. 42, no. 4, pp. 432–445, May 2014.

[Bayat 2008] D. Bayat, T. Akiyama, N. F. de Rooij, and U. Staufer. (2008) "Dynamic behavior of the tuning fork AFM probe," *Microelectron. Eng.*, vol. 85, no. 5–6, pp. 1018–1021, May.

[Busby 2018] Y. Busby, A. Franquet, V. Spampinato, G. Casula, A. Bonfiglio, P. Cosseddu, J.J. Pireaux, L. Houssiau, Combined AFM and ToF-SIMS analyses for the study

of filaments in organic resistive switching memories. Proc. SPIE 10738, Organic and Hybrid Sensors and Bioelectronics XI, 1073814 (2018). DOI: 10.1117/12.2319923

[Casula 2019] Casula, G., Busby, Y., Franquet, A., Spampinato, V., Houssiau, L., Bonfiglio, A., Cosseddu, P., A flexible organic memory device with a clearly disclosed resistive switching mechanism. Organic Electronics, Volume 64, (2019): 209-215. DOI: 10.1016/j.orgel.2018.10.018

[Dunn 1999] D. N. Dunn and R. Hull. (1999). "Reconstruction of three-dimensional chemistry and geometry using focused ion beam microscopy," *Appl. Phys. Lett.*, vol. 75, no. 21, pp. 3414–3416

[Giannuzzi 2005] L. A. Giannuzzi and F. A. Stevie. (2005), *Introduction to Focussed Ion Beams. Instrumentation, Theory,Techniques and Practice*. Springer.

[Giannuzzi 2011] L. A. Giannuzzi and M. Utlaut. (2011), "A review of Ga+ FIB/SIMS," *Surf. Interface Anal.*, vol. 43, no. 1–2, pp. 475–478.

[Jeans 2009] J. Jeans (2009), "PREFACE," in *An Introduction to the Kinetic Theory of Gases*, Cambridge: Cambridge University Press, pp. ix–x.

[Kushmeric 2016] J. G. Kushmerick and P. S. Weiss. (2016), *Scanning Probe Microscopes*.

[Lyytikäinen 2009] J. Lyytikäinen, J. Rautiainen, L. Toikkanen, A. Sirbu, A. Mereuta, A. Caliman, E. Kapon, O.G. Okhotnikov. (2009) "1.3-Microm Optically-Pumped Semiconductor Disk Laser By Wafer Fusion.," *Opt. Express*, vol. 17, no. 11, pp. 9047–9052.

[Nečas 2012] D. Nečas, P. Klapetek (2012), "Gwyddion: An open-source software for SPM data analysis," *Cent. Eur. J. Phys.*, vol. 10, no. 1, pp. 181–188.

[Noel 2019] C. Noel, S. Pescetelli, A. Agresti, A. Franquet, V. Spaminato, A. Felten, A. di Carlo, L. Houssiau, Y. Busby, Hybrid Perovskites depth profiling with variable-size argon clusters and monatonic ions beams. Materials (2019) 12 (5) 726. DOI:

10.3390/ma12050726

[Perez-Cruz2012]: A. Perez-Cruz, A. Dominguez-Gonzalez, I. Stiharu, R.A. Osornio-Rios, Optimization of Q-factor of AFM cantilevers using genetic algorithms. Ultramicroscopy 115(2012):61-67

[Pillatsch 2018] L. Pillatsch, Fredrik Östlund, and J. Michler. (2019), "FIBSIMS A review of secondary ion mass spectrometry for analytical dual beam focussed ion beam instruments," *Prog. Cryst. Growth Charact. Mater.*, no. xxxx, pp. 1–19

[Priebe 2019] A. Priebe, J.-P. Barnes, T.E.J. Edwards, L. Pethö, I. Balogh, and J. Michler. (2019) "3D Imaging of Nanoparticles in an Inorganic Matrix Using TOF-SIMS Validated with STEM and EDX," *Anal. Chem.*, vol. 91, no. 18, pp. 11834–11839.

[Rodríguez 2003] T. R. Rodríguez and R. García. (2003), "Theory of Q control in atomic force microscopy," *Appl. Phys. Lett.*, vol. 82, no. 26, pp. 4821–4823.

[Wei 2008] Q. Wei, J. Lian, W. Lu, and L. Wang. (2008), "Highly ordered Ga nanodroplets on a GaAs surface formed by a focused ion beam," *Phys. Rev. Lett.*, vol. 100, no. 7, pp. 20–23.

[Whitby 2012] J. A. Whitby, F. Östlund, P. Horvath, M. Gabureac, J.L. Riesterer, I. Utke, M. Hohl, L. Sedláček, J. Jiruše, V. Friedli, M. Bechelany, J Michler. (2012) "High Spatial Resolution Time-of-Flight Secondary Ion Mass Spectrometry for the Masses: A Novel Orthogonal ToF FIB-SIMS Instrument with In Situ AFM," *Adv. Mater. Sci. Eng.*, pp. 1–13.

Figure Legends

Figure 1: HV AFM setup with the sample installed on the 10 μm × 10 μm range scanning table. The adjustment of the tip height is done by a piezo manipulator below the tip. Coarse motions to position the tip at the area of interest are realized by slip stick nanomanipulators. The inset picture shows a secondary electron image of the tip close to the surface.

Figure 2: a) Layer structure of the VCSEL sample composed by 5 times a set of an aluminium rich layer structure separated by an indium phosphide (InP) layer, followed by 35 times alternating gallium arsenide (GaAs) and aluminium gallium arsenide (AlGaAs) layer structure. b) SIMS depth profile of the VCSEL sample showing the Al-rich structure and one of the AlGaAs layers.

Figure 3: a) Centering of the tip in the SIMS crater to calibrate the zero level of the AFM tip. b) SIMS-AFM scanning strategy. After the SIMS data acquisition, the roughness of the sputtered crater is scanned by AFM (Area 1). In a second scan (Area 2), the crater edge is scanned in order to determine the crater depth. c) AFM depth profile (z) as a function of in-plane position (x), crater roughness and the ^{27}Al distribution measured by SIMS are represented.

Figure 4: Effect of surface oxidation on the recombined depth profile of the ^{27}Al, ^{69}Ga and ^{115}In SIMS signal. At every 20th SIMS frames, sputtering is interrupted for an AFM scan. The effect of surface oxidation during the AFM scan is visible by the enhanced secondary ion signal at the first SIMS frame after the AFM scan. Data correction is done by averaging the SIMS signal over the last SIMS scan before and the second SIMS scan after an AFM scan.

Figure 5: Top graph: Roughness and crater depth evolution as a function of the number of SIMS frames. Bottom graph: the ^{27}Al, ^{69}Ga and ^{115}In depth profile is shown and related to the depth information measured by AFM. The sputter rates of ^{27}Al-rich layer structures are evaluated in terms of sputter depth. Data of the graph is provided in Supplementary Table 1.

Figure 6: Overlay of the depth-corrected ^{27}Al signal with the original ^{27}Al signal plotted as a function of sputter time.

Figure 7: a-i) Surface roughness development from AFM scans 18 to 26. The RMS roughness values change due to globular nanostructure formation at the interfaces of the GaAs/AlGaAs layer. For the AFM pictures, the 8 µm× 8 µm middle part of the crater is shown. AFM height measurement at the crater edges are influenced by the dimensions of the AFM tip. The same globular nanostructure at the crater bottom is visible at the SEM picture taken after the last AFM scan (j), while no local increase in ^{69}Ga could have been observed on SIMS images during the nanostructure-formation (k).

Figure 8: Sketch of the 3D model build-process based on variable number of ToF-SIMS frames. a) Slices used for the 3D reconstruction of the sample, b) Each slice consists of 20 nm thick layers, the amount of layers is adapted to the average sputter depth of one slice. c) An example showing that the 3D slices were constructed for the different ions, in this case ^{27}Al.

Figure 9: AFM Depth-corrected 3-dimensional distribution of ^{27}Al, ^{69}Ga and ^{115}In ions. X and Y axes correspond to 5 µm lateral length, Z axis has been lengthened 6 times for better visualization, as in

reality it only corresponds to 1.1 µm depth. Combination of the three ions were projected onto one another to emphasize similarities in their spatial distribution.

Figures

Figure 1

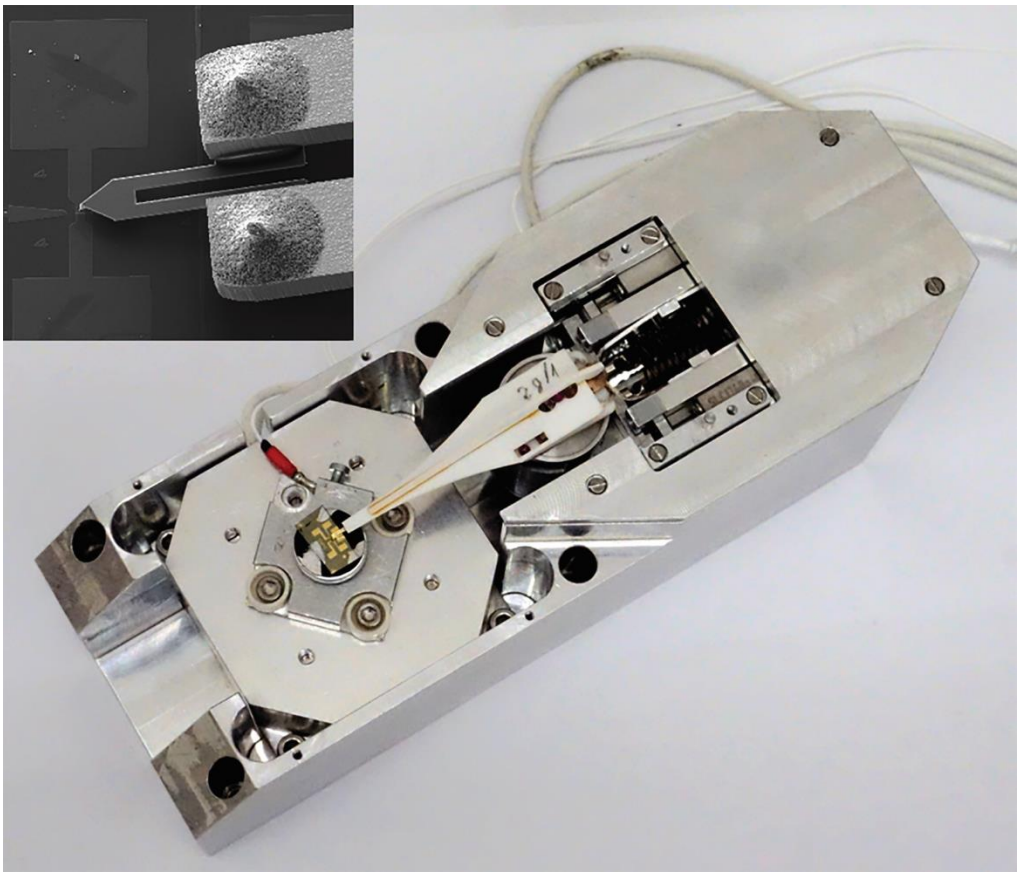

Figure 2

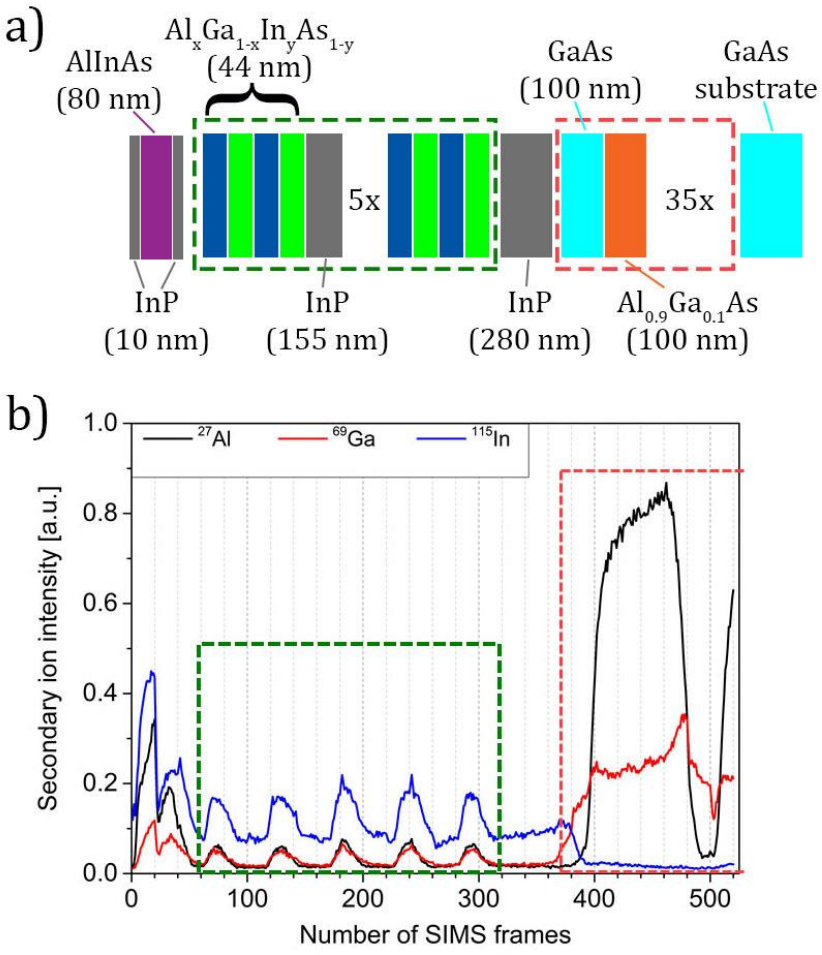
a)
AlInAs
(80 nm)
$Al_xGa_{1-x}In_yAs_{1-y}$
(44 nm)
GaAs
(100 nm)
GaAs
substrate
5x
35x
InP
(10 nm)
InP
(155 nm)
InP
(280 nm)
$Al_{0.9}Ga_{0.1}As$
(100 nm)
b)
^{27}Al
^{69}Ga
^{115}In
Secondary ion intensity [a.u.]
Number of SIMS frames
0.0
0.2
0.4
0.6
0.8
1.0
0
100
200
300
400
500

Figure 3

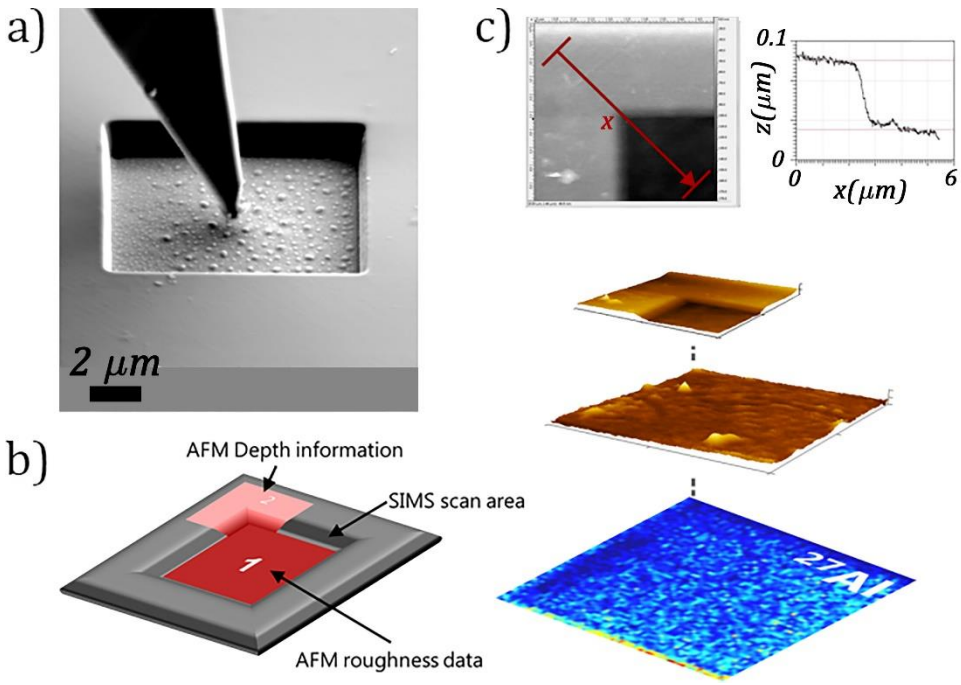
a)
2 μm
c)
x
0.1
z(μm)
0
0
x(μm)
6
b)
AFM Depth information
SIMS scan area
1
2
AFM roughness data
27 A

Figure 4

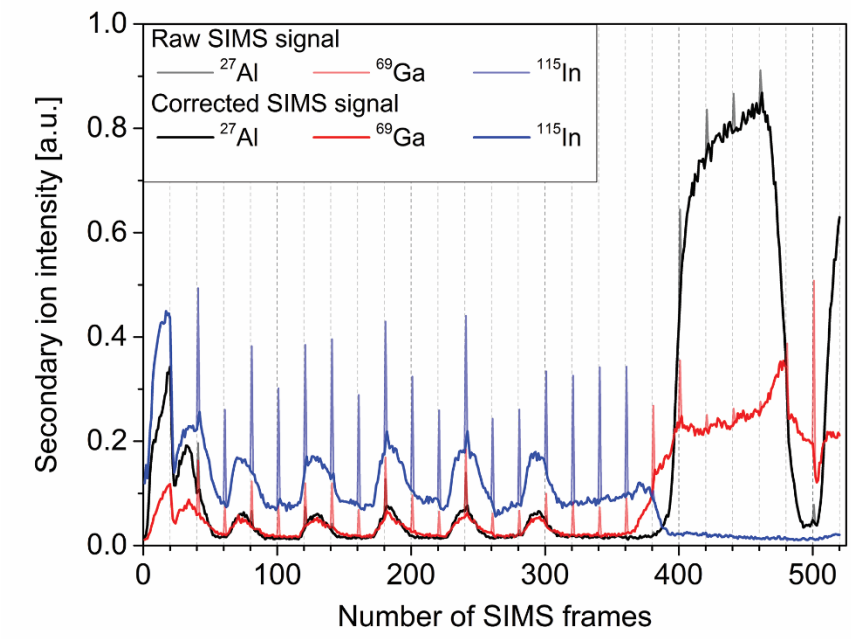
Raw SIMS signal
27Al
69Ga
115In
Corrected SIMS signal
27Al
69Ga
115In
Secondary ion intensity [a.u.]
Number of SIMS frames
0.0
0.2
0.4
0.6
0.8
1.0
0
100
200
300
400
500

Figure 5

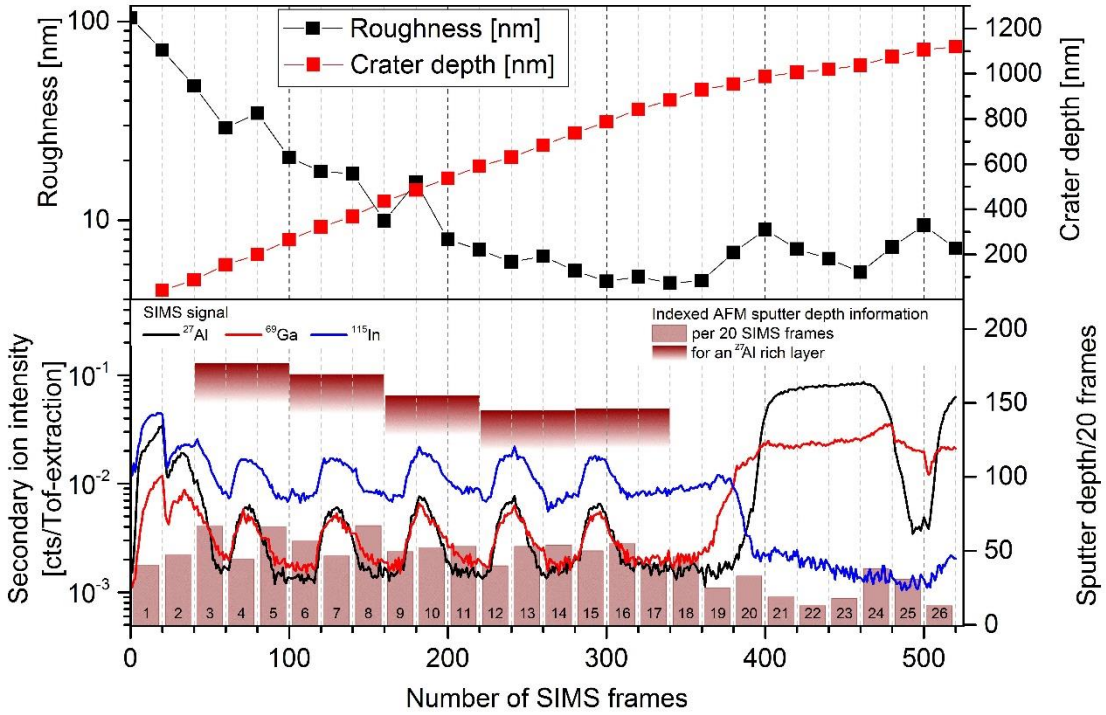
Roughness [nm]
Crater depth [nm]
Roughness [nm]
Crater depth [nm]
SIMS signal
27Al
69Ga
115In
Indexed AFM sputter depth information
per 20 SIMS frames
for an 27Al rich layer
Secondary ion intensity [cts/Tof-extraction]
Sputter depth/20 frames
Number of SIMS frames

Figure 6

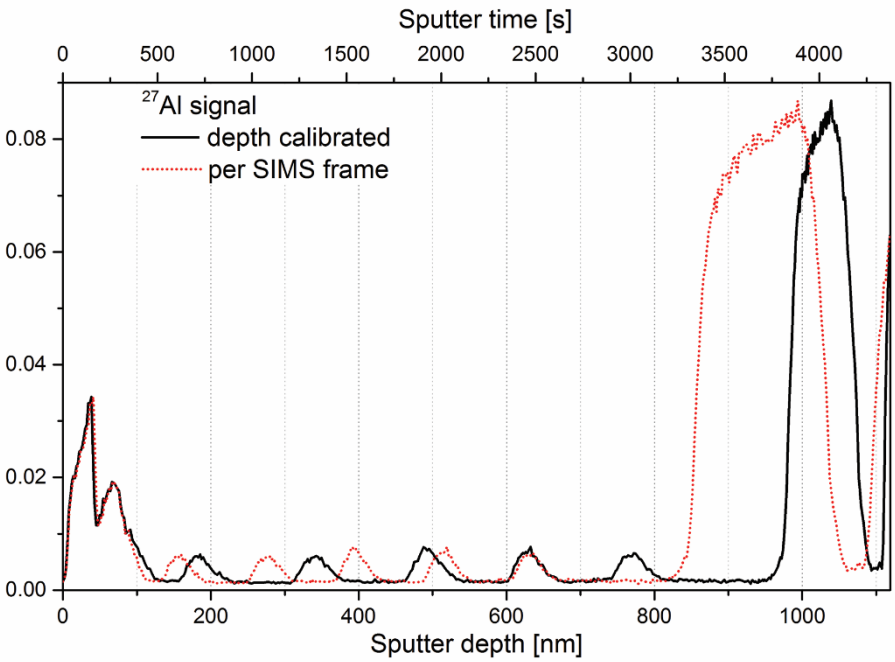
Sputter time [s]
0
500
1000
1500
2000
2500
3000
3500
4000
27Al signal
depth calibrated
per SIMS frame
0.08
0.06
0.04
0.02
0.00
0
200
400
600
800
1000
Sputter depth [nm]

Figure 7

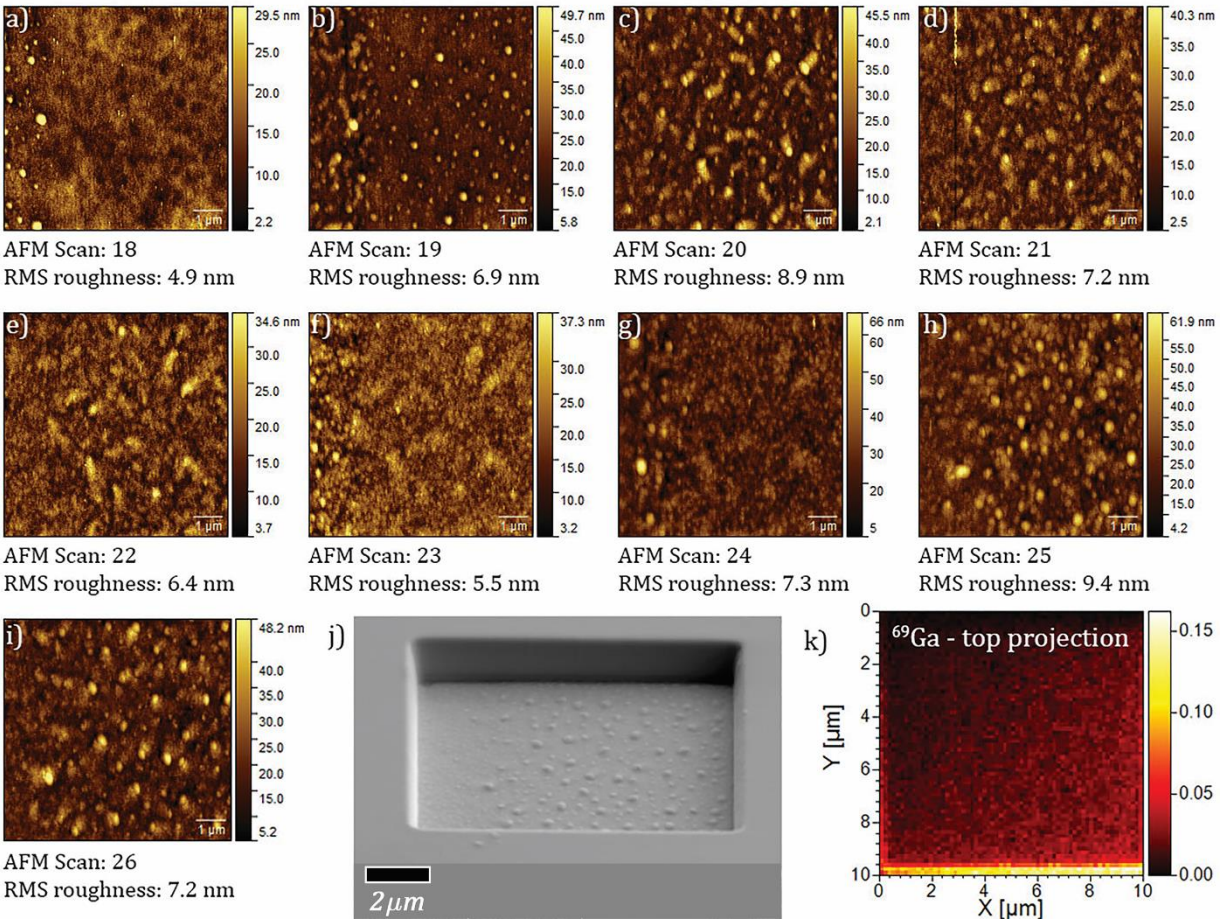
a)
29.5 nm
25.0
20.0
15.0
10.0
2.2
1 µm
AFM Scan: 18
RMS roughness: 4.9 nm
b)
49.7 nm
45.0
40.0
35.0
30.0
25.0
20.0
15.0
5.8
1 µm
AFM Scan: 19
RMS roughness: 6.9 nm
c)
45.5 nm
40.0
35.0
30.0
25.0
20.0
15.0
10.0
2.1
1 µm
AFM Scan: 20
RMS roughness: 8.9 nm
d)
40.3 nm
35.0
30.0
25.0
20.0
15.0
10.0
2.5
1 µm
AFM Scan: 21
RMS roughness: 7.2 nm
e)
34.6 nm
30.0
25.0
20.0
15.0
10.0
3.7
1 µm
AFM Scan: 22
RMS roughness: 6.4 nm
f)
37.3 nm
30.0
25.0
20.0
15.0
10.0
3.2
1 µm
AFM Scan: 23
RMS roughness: 5.5 nm
g)
66 nm
60
50
40
30
20
5
1 µm
AFM Scan: 24
RMS roughness: 7.3 nm
h)
61.9 nm
55.0
50.0
45.0
40.0
35.0
30.0
25.0
20.0
15.0
4.2
1 µm
AFM Scan: 25
RMS roughness: 9.4 nm
i)
48.2 nm
40.0
35.0
30.0
25.0
20.0
15.0
5.2
1 µm
AFM Scan: 26
RMS roughness: 7.2 nm
j)
2 µm
k)
69Ga - top projection
Y [µm]
X [µm]
0
2
4
6
8
10
0.15
0.10
0.05
0.00

Figure 8

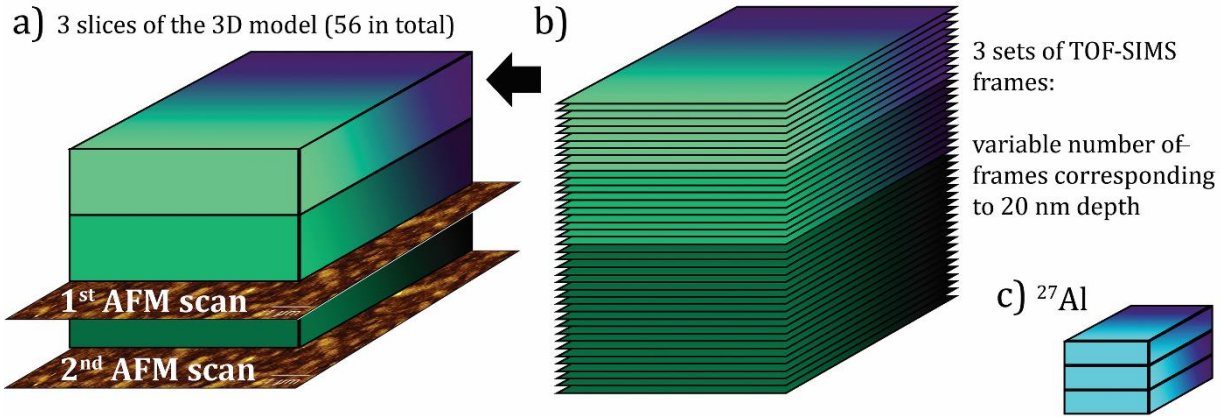
a) 3 slices of the 3D model (56 in total)
b)
3 sets of TOF-SIMS frames:
variable number of frames corresponding to 20 nm depth
c) ^{27}Al
1st AFM scan
2nd AFM scan
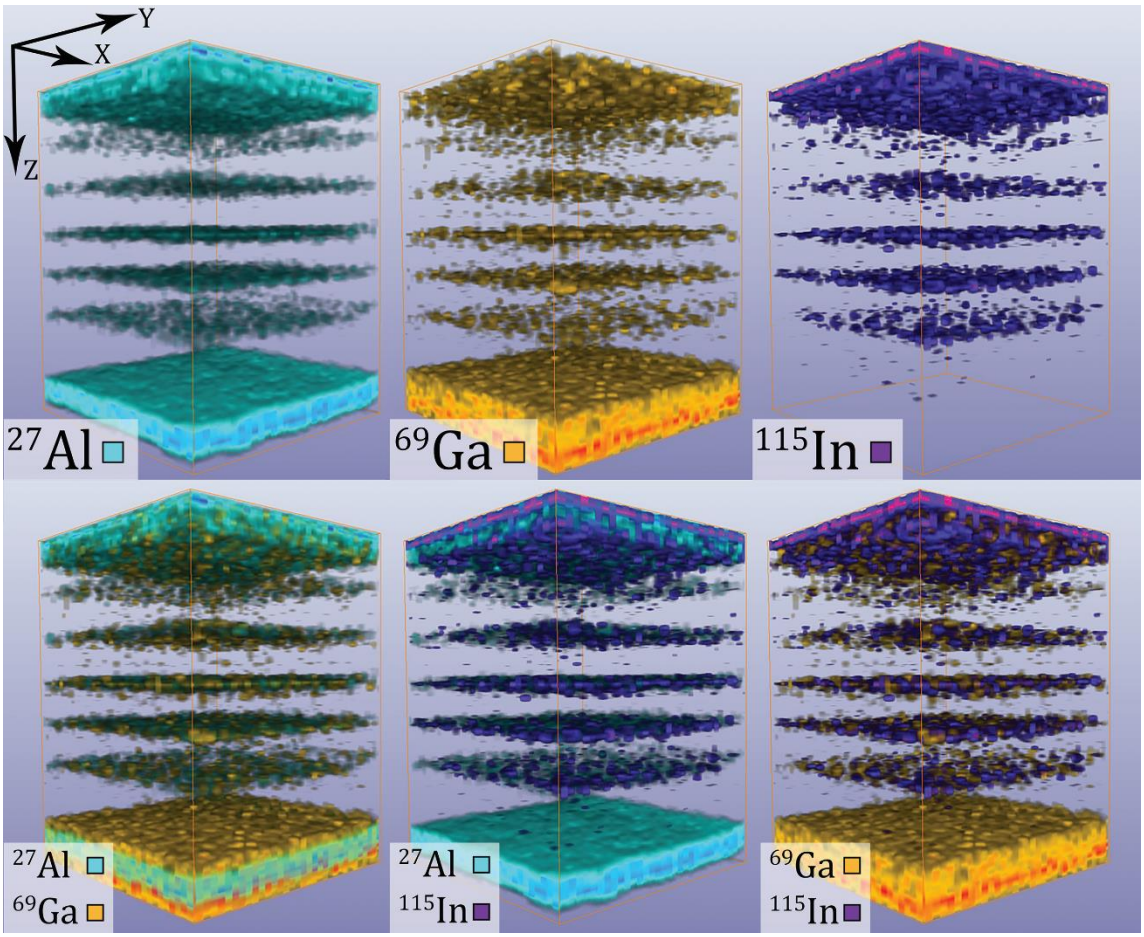
Figure 9